Supplementary Materials for

An unusually delayed and persistent atmospheric CO_2 response to the 2023/24 El Niño

Xiaoyu Sun et al.

*Corresponding author. Email: Xiaoyu_sun@iup.physik.uni-bremen.de and jnotholt@iup.physik.uni-bremen.de

This PDF file includes:

Supplementary Text

Figs. S1 to S9

Tables S1 to S9

Supplementary Text

S1 Event-aligned atmospheric CO_2-growth methods and sensitivity

S1.1 Data and event alignment

We quantified atmospheric timing and peak-aligned post-peak persistence using ONI-peak alignment. Lag 0 was the central month of the maximum ONI season for each of 12 selected events. The full event set comprised 1982/83, 1987/88, 1991/92, 1994/95, 1997/98, 2002/03, 2004/05, 2006/07, 2009/10, 2015/16, 2018/19, and 2023/24. The primary strong-event comparison comprised 1987/88, 1997/98, 2009/10, 2015/16, and 2023/24. The 1982/83 and 1991/92 cases are volcanically confounded and descriptive only; 2018/19 is a moderate, low-amplitude persistence diagnostic excluded from the strong-event ranking.

For monthly atmospheric CO_2 concentration C(t), centered 12-month growth was G(t) = C(t+6) − C(t−6), in ppm yr−1. The first and last six months of the concentration record were unavailable for this centered calculation.

$$G_c(t) = C^*(t+6) - C^*(t-6) \tag{1}$$

For the primary analysis, all months from lag −6 through +21 around the 12 selected peaks were masked when estimating the low-frequency background. A robust local-linear LOWESS fit with a fixed 120-month nearest-neighbor span was estimated from the unmasked months and predicted through the masked event windows.

$$\overline{G_c}(m) = \frac{1}{N_m} \sum_{t:m(t)=m} G_c\,(t), \tag{2}$$

mask(t) denote that prediction. The residual R(t) = G(t) − m(t) was formed, its calendar-month climatology was calculated from the full residual series, and the primary anomaly was A(t) = R(t) – climatology month(t). This final step removes residual calendar-month dependence after low-frequency detrending.

The event-masked LOWESS anomaly was selected because it minimized event-window signal absorption among the detrended methods and showed the strongest endpoint and leave-one-event-out stability. Selection was based on fitting diagnostics, not event rankings. The current anomaly definition, which subtracts a calendar-month climatology from G(t) without low-frequency detrending, was retained only as a sensitivity and therefore retains low-frequency changes in atmospheric CO_2 growth.

S1.2 Definitions of peak lag and effective post-peak duration

For event e with peak month t_e, $A_e(\ell) = A(t_e+\ell)$. The post-peak maximum is the maximum $A_e(\ell)$ in the evaluated window, and peak lag is the month of that maximum relative to lag 0.

$$A_{\max} = \max_{t\geq 0} A(t), \tag{4}$$

For threshold α ∈ {0.25, 0.33, 0.50}, the threshold is α times the event's own post-peak maximum.

$$A(t) \geq \alpha A_{\max}. \tag{5}$$

The effective post-peak duration begins at the first post-peak month at or above threshold.

t_start,α = min{t ≥ 0 : A(t) ≥ αA_max}, (6) It ends immediately before the first month belonging to a run of at least two consecutive below-threshold months. One isolated below-threshold month does not terminate the response.

The effective duration was then calculated as

$$D_\alpha = t_{end,\alpha} - t_{start,\alpha} + 1, \qquad (7)$$

D0.25, D0.33, and D0.50 are peak-aligned effective post-peak duration, or persistence, metrics; they are not measures of complete ecosystem recovery. A response without a qualifying endpoint by lag +21 is reported as right-censored.

D0.50 was used in the primary comparison, with D0.25 and D0.33 as threshold-sensitivity tests.

S1.3 Threshold sensitivity

Under event-masked LOWESS, 2023/24 had D0.25/D0.33/D0.50 = 12/11/10 months. Its D0.50 was second among the selected strong events after 1997/98 (11 months), and longer than 2015/16 (6 months). The relative-threshold metrics describe peak-aligned persistence and must be interpreted with amplitude. The moderate 2018/19 response illustrates that a low-amplitude response can still have measurable persistence.

S1.4 Peak lag and cumulative metrics

Peak lag is the month of the maximum post-peak detrended CO_2-growth anomaly relative to lag 0. It measures timing, not persistence or ecosystem recovery.

$$L_{\text{peak}} = \arg\max_{t\geq 0} A(t)\,, \qquad (8)$$

For an integration length T, $I_T = \Sigma[\ell=0 \text{ to } T-1]\, A_e(\ell)/12$. All positive and negative monthly values are included. I18 uses lags 0–17 and is expressed in ppm; it is the detrended cumulative post-peak CO_2-growth anomaly, not CO_2 emissions attributable to El Niño.

The 2023/24 maximum occurred at lag +7, later than 1997/98 (+4) and 2015/16 (+2). Its I18 was 0.885 ppm, third among the selected strong events after 1997/98 (1.361 ppm) and 1987/88 (0.993 ppm), and approximately twice 2015/16 (0.431 ppm).

The August 1987 lag-0 assignment corresponds to JAS 1987 and a unique maximum ONI of 1.70°C; it is not a tie-breaking artifact.

The primary results distinguish 2023/24 by its latest peak and unusually persistent response relative to lower forcing, not by a historical-number-one cumulative ranking.

S1.5 Strong-event rankings and integration-window sensitivity

For event-masked LOWESS, strong-event D0.50 ranked 1997/98 (11), 2023/24 (10), 1987/88 (7), 2015/16 (6), and 2009/10 (5 months). I18 ranked 1997/98 (1.361), 1987/88 (0.993), 2023/24 (0.885), 2015/16 (0.431), and 2009/10 (−0.075 ppm). Common coverage extends through lag +21. I12, I15, and I21 were sensitivity tests; 2023/24 remained later and cumulatively larger than 2015/16 across the tested windows.

S1.6 Background-method sensitivity

Sensitivity backgrounds included the current calendar-month-centered anomaly, linear, quadratic, cubic, and quartic trends, conventional 10-year LOWESS, event-masked 10-year LOWESS, and a GCV cubic spline diagnostic. The current definition removes residual calendar-month dependence but retains low-frequency changes. Conventional LOWESS and higher-order polynomial fits absorbed appreciable event-scale variability near 1987/88 and 2023/24. Under the current definition, 2023/24 had the largest strong-event I18 (1.880 ppm) and longest strong-event D0.50 (12 months), but those absolute rankings were not robust to low-frequency background removal.

S1.7 Fitting diagnostics

Event-masked LOWESS used 215 unmasked months and had residual variance 0.294286 and lag-1 autocorrelation 0.935415. When 2023/24 was omitted, its mean absorbed background was 0.023 ppm yr^{-1}, maximum absolute background difference 0.029 ppm yr^{-1}, I18 change +0.034 ppm, and D0.50 remained 10 months. Endpoint trims changed its I18 by −0.003 to −0.006 ppm while D0.50 remained 10 months. These diagnostics showed smaller event-window absorption and stronger stability than the other detrended approaches.

S1.8 GCV spline diagnostic

The GCV-selected cubic spline used $\lambda = 0.00398107$ and approximately 48.057 effective degrees of freedom. It followed event-scale peaks, sharply reduced residual variance, and was unstable under event omission and endpoint trimming. It was therefore rejected as an overfit and unsuitable low-frequency background, irrespective of the rankings it produced.

S1.9 Robust interpretation

Across reasonable detrending methods, the robust contrast is that the 2023/24 response was later, more persistent, and cumulatively larger than the response following 2015/16. The audit does not support describing 2023/24 as the largest detrended historical response or as having the longest strong-event D0.50 under the primary background.

S2 Tropical Pacific station evidence for sustained annual CO_2 growth

To assess whether the sustained post-peak CO_2-growth response was also detectable in independent in situ observations over the tropical Pacific, we analyzed atmospheric CO_2 records for American Samoa (SAM) and Cape Kumukahi (KUM) obtained from the Scripps CO_2 Program (36). Mauna Loa (MLO) was included as a separate long-term reference record identified in the main Methods and Data availability as NOAA GML data. This independent station-based evidence supports the interpretation that enhanced CO_2 growth persisted over the tropical Pacific in the year following the 2023/24 El Niño peak. MLO also shows elevated growth in 2025, but is used here mainly as a long-term reference rather than as part of the tropical Pacific stations.

For each station, annual CO_2 growth was calculated as the year-to-year difference in full-calendar-year annual mean CO_2 concentration,

$$G_{s,y} = \overline{C_{s,y}} - \overline{C_{s,y-1}}, \tag{9}$$

where s denotes the station and y is the ending year. Only years with complete January–December monthly records in both the target year and the preceding year were used.

For each selected El Niño event, we define Y1 as the ONI peak year and Y2 as the following post-peak year.

Annual CO2 growth at tropical Pacific background stations is shown in fig. S1 and the values of the growth rates during the peak and the post-peak year of the El Niño events since 1980 are shown in Table S6.

The two tropical Pacific stations show high annual CO_2 growth in 2025, reaching 3.87 ppm yr^{-1} at SAM and 3.89 ppm yr^{-1} at KUM. These values are substantially higher than the previous selected-event (Y2) ranges of 1.52–2.41 ppm yr^{-1} at SAM and 1.45–2.51 ppm yr^{-1} at KUM (Table S6).

To test whether the tropical Pacific station growth was elevated relative to the global background, we also calculated a station-minus-global annual growth anomaly,

$$R_s(y) = G_{s,y} - G_{\text{global},y}, \tag{10}$$

where $G_{s,y}$ is the station annual CO_2 growth rate and $G_{\text{global},y}$ is the NOAA global annual CO_2 growth rate for the same ending year. Positive $R_s(y)$ indicates that the station growth exceeds the global mean growth. The time series of the $R_s(y)$ is shown in fig. S1C. In 2025, the anomaly reached 1.75 ppm yr^{-1} at SAM and 1.77 ppm yr^{-1} at KUM, showing that the elevated tropical Pacific growth in 2025 was not only high in absolute terms but also enhanced relative to the global annual growth background.

S3 Palau EM27/SUN observations and growth-rate estimates

S3.1 Palau EM27/SUN observations and sampling

Atmospheric column CO_2 at Palau was measured using an EM27/SUN Fourier transform infrared spectrometer operated at the Palau Atmospheric Observatory in the tropical western Pacific (7.3°N, 134.5°E; Fig. S2). The instrument is part of the COllaborative Carbon Column Observing Network (COCCON) (39, 40) and records direct-sun near-infrared spectra, from which column-averaged dry-air mole fractions of CO_2, XCO_2, are retrieved.

The Palau site is located in the western Pacific warm-pool region and provides a ground-based column-CO_2 constraint close to the GOSAT western Pacific averaging domain used in this study. Fig. S2A shows the Palau EM27/SUN site, the GOSAT western Pacific domain, the Niño 3.4 region, and reference background CO_2 stations used elsewhere in the analysis.

Because EM27/SUN observations require direct sunlight and sufficiently clear-sky conditions, the monthly sampling is uneven. We therefore document, for each month, the number of independent observation days, unique local observation hours, total observation span, and retrieval counts (Fig. S3a). Monthly means were calculated from quality-screened retrievals using equal-day weighting, so that days with many retrievals do not dominate the monthly mean. Local observation times were expressed in Palau local time.

The Palau EM27/SUN record currently spans 2024–2025 and is too short to define a fully independent long-term climatological XCO_2 anomaly comparable to the GOSAT, Mauna Loa, or NOAA global mean records. We therefore use the Palau data as an independent ground-based consistency check for the post-El Niño CO_2 enhancement in 2025, rather than as the primary constraint on the long-term anomaly or response duration.

S3.2 Palau residual-growth and uncertainty estimate used in Fig. 2c

Rationale

The Palau EM27/SUN record provides direct ground-based column observations over the tropical western Pacific, but the record length is not sufficient to estimate a local climatological anomaly in the same way as for the longer satellite or background-station records. To use the Palau observations without over-interpreting them as a standalone anomaly record, we define a matched-month residual-growth metric.

Definition

For each calendar month with observations in both 2024 and 2025, we first calculated the Palau matched-month growth:

$$G_{Palau}(m) = XCO_{2,Palau}(2025, m) - XCO_{2,Palau}(2024, m), \tag{11}$$

where m denotes the calendar month. Because the comparison is made between the same calendar month in two consecutive years, this quantity represents the one-year XCO_2 growth at Palau for that month.

The corresponding western Pacific background growth was calculated from the GOSAT Tropical Western Pacific (TWP) regional (5°S–5°N, 120°E–180°E) record:

$$G_{GOSAT,TWP}(m) = XCO_{2,GOSAT,TWP}(2025, m) - XCO_{2,GOSAT,TWP}(2024, m), \tag{12}$$

The Palau residual growth was then defined as:

$$R_{\text{Palau}}(m) = G_{Palau}(m) - G_{GOSAT,TWP}(m), \tag{13}$$

where $R_{\text{Palau}}(m)$ represents the remaining Palau growth after subtracting the regional TWP background growth. The GOSAT western Pacific record was used as the background reference and represents the regional column-CO_2 environment around the Palau site.

This residual metric is not a local flux estimate and is not equivalent to a long-term climatological anomaly. Instead, it provides a short-record, site-level comparison with the regional GOSAT background. In this sense, the Palau residual growth and the GOSAT long-term anomaly are conceptually related: both remove the mean seasonal cycle and the background atmospheric CO_2 increase, and therefore emphasize the interannual component of the post-El Niño perturbation.

Sampling and uncertainty

All available matched months were retained in Fig. 1B and Fig. 2C. No month was excluded based on the sign or magnitude of the residual-growth estimate. The Palau monthly uncertainty was estimated from the variability of daily means within each month. For months with only one independent observation day, a conservative fallback uncertainty was assigned using the median daily-mean uncertainty derived from multi-day Palau months. The uncertainty in the Palau matched-month growth was then calculated by propagating the 2024 and 2025 monthly uncertainties.

For each matched month, the uncertainty in the Palau matched-month growth was calculated as

$$\sigma_{\Delta\text{palau}}(m) = \sqrt{\sigma^2_{\Delta\text{Palau}}(2025, m) + \sigma^2_{\Delta\text{Palau}}(2024, m)}. \tag{14a}$$

The uncertainty of the residual-growth estimate additionally includes the uncertainty in the GOSAT western Pacific background growth:

$$\sigma_{\text{residual}} = \sqrt{\sigma^2_{\Delta\text{Palau}}(m) + \sigma^2_{\Delta\text{GOSAT,WP}}(m)}. \tag{14b}$$

Role in the main interpretation

The Palau residual-growth estimate is used only as an auxiliary ground-based consistency check. It is not used to define the duration of the post-El Niño atmospheric CO_2 response. The persistence and timing of the broader atmospheric signal are evaluated primarily from the continuous GOSAT, NOAA global mean, Mauna Loa, and background-station records.

The residual-growth formulation is useful because it separates two quantities that have different interpretations. The total Palau matched-month growth indicates how much XCO_2 increased at

Palau between 2024 and 2025. The Palau residual growth indicates how much of that increase remains after subtracting the regional GOSAT western Pacific background growth. Thus, the residual points in Fig. 2C provide a conservative site-level test of whether the Palau measurements show additional enhancement relative to the regional western Pacific background.

S3.3 Palau matched-month annual growth estimate used in Fig. 1B

The Palau point shown in Fig. 1B represents the available-month annual growth between 2024 and 2025, rather than a full calendar-year annual mean. This choice is necessary because the Palau EM27/SUN record does not yet provide multiple complete years from which a conventional annual climatology or deseasonalized annual mean can be derived.

We define the Palau matched-month annual growth as the arithmetic mean of the year-to-year XCO_2 differences for all calendar months with valid observations in both 2024 and 2025:

$$G_{Palau}^{2025} = \frac{1}{N} \sum_{m \in M} [XCO_{2,Palau}(2025, m) - XCO_{2,Palau}(2024, m)], \tag{15}$$

where M is the set of matched months and N is the number of matched months. In the calculation, the matched months are February, March, April, May, June, August, September, October, and November.

The uncertainty of the matched-month annual growth was propagated from the monthly sampling uncertainties.

S3.4 Sensitivity tests

We performed several sensitivity tests to evaluate whether the Palau matched-month annual growth estimate depends strongly on sampling choices, monthly weighting, or individual months (Table S7). The default calculation uses equal-day-weighted monthly means and all matched months, giving a Palau matched-month annual growth of 3.36 ± 0.09 ppm yr^{-1}.

Using retrieval-weighted monthly means instead of equal-day-weighted monthly means gives 3.29 ppm yr^{-1}, only 0.07 ppm lower than the default estimate. This indicates that the annual growth estimate is not strongly affected by days or months with larger retrieval counts.

Restricting the calculation to robust months, defined as months with at least two independent observation days in both 2024 and 2025, gives 3.25 ± 0.23 ppm yr^{-1}. This estimate is based only on March and October and is therefore less representative seasonally, but it remains close to the default value. This result indicates that including low-count months does not artificially create the enhanced Palau growth signal.

Using only months available through August 2025 gives 3.52 ± 0.13 ppm yr^{-1}, slightly higher than the all-month default estimate. This shows that the enhanced Palau growth is already evident before the later low-count months are included.

Leave-one-month-out tests give values between 3.17 and 3.48 ppm yr^{-1}. The largest shift occurs when May is excluded, but the estimate remains above 3 ppm yr^{-1} in all cases. Thus, the Palau matched-month annual growth estimate is not controlled by a single month.

Overall, the sensitivity tests show that the Palau matched-month annual growth remains elevated across reasonable sampling and weighting choices. These tests support the use of Palau as an independent ground-based consistency check for enhanced 2025 CO_2 growth, while also emphasizing that the short and unevenly sampled Palau record should not be interpreted as a standalone long-term anomaly record.

S4 GOSAT XCO_2 processing and uncertainty propagation

S4.1 Retrieval screening and regional aggregation

GOSAT XCO_2 observations were obtained from the Level-2 Short-Wavelength Infrared product SWIRL2CO2_GU version 03.05 (37, 38). The record analyzed here spans April 2009 to December 2025. For each sounding, we extracted the bias-corrected XCO_2 value and its reported retrieval uncertainty.

Retrievals were screened using the recommended post-screening quality indicators, including the physically plausible XCO_2 range, solar zenith angle, degrees of freedom for signal, land fraction, and the post-screening quality flag. Only retrievals passing the complete post-screening procedure were retained. A minimum uncertainty of 0.1 ppm was imposed before inverse-variance weighting to prevent anomalously small reported uncertainties from producing disproportionate statistical weights.

Regional means were calculated for Niño3.4 (5°S–5°N, 170°W–120°W), the tropical western Pacific (5°S–5°N, 120°E–180°E), and the tropical-Pacific and global domains used in Fig. 3. The complete regional definitions are listed in Table S8.

Within each region, valid soundings were first aggregated by observation day using inverse-variance weights

$$w_i = \frac{1}{\sigma_i^2}, \quad (17)$$

where X_i and σ_i denote the bias-corrected XCO_2 retrieval and its reported uncertainty, respectively. The weighted daily mean was

$$\bar{X}_d = \frac{\sum_{i\in d} w_i X_i}{\sum_{i\in d} w_i}. \quad (18)$$

Daily values were subsequently aggregated to monthly regional means using the same inverse-variance framework. The standard error associated with each monthly mean was retained for the anomaly fitting and bootstrap uncertainty analysis.

S4.2 Polynomial–harmonic anomaly calculation

Monthly XCO_2 anomalies were calculated after removing the fitted long-term increase and mean seasonal cycle from each regional time series. Time was expressed in fractional years, and the following polynomial–harmonic model was fitted over April 2009 to December 2025:

$$\hat{X}_{CO_2}(t) = a_0 + a_1 t + a_2 t^2 + \sum_{k=1}^{2} [b_k \sin(2\pi k t) + c_k \cos(2\pi k t)], \quad (19)$$

where a_0, a_1, and a_2 describe the long-term background evolution. The terms with $k = 1$ and $k = 2$ represent the annual and semiannual cycles, respectively.

The monthly anomaly was calculated as

$$X'_{CO_2}(t) = X_{CO_2}(t) - \hat{X}_{CO_2}(t). \quad (20)$$

The same fitting structure and study period were used for all GOSAT regions so that differences among the Niño3.4, western-Pacific, tropical-Pacific, and global records were not introduced by different detrending procedures.

S4.3 Bootstrap propagation of monthly sampling uncertainty

Uncertainty in the fitted XCO_2 anomaly was estimated using 1000 parametric bootstrap realizations. For each realization r, every available monthly regional mean was sampled as

$$X_{CO_2}^{(r)}(t_i) \sim \mathcal{N}\left[X_{CO_2}(t_i), \mathrm{SEM}_X(t_i)^2\right], \qquad (21)$$

where $X_{CO_2}(t_i)$ is the observed regional monthly mean and $\mathrm{SEM}_X(t_i)$ is its estimated standard error. Missing months were retained as missing and were not interpolated.

The complete polynomial–harmonic model was independently refitted to each bootstrap realization, and the corresponding anomaly was calculated as

$$X_{CO_2}^{\prime(r)}(t) = X_{CO_2}^{(r)}(t) - \hat{X}_{CO_2}^{(r)}(t). \qquad (22)$$

The anomaly calculated from the unperturbed monthly means was used as the central estimate. At each month, the 16th and 84th percentiles of the 1000 bootstrap anomalies define the pointwise 68% uncertainty interval shown in Figs. 2 and 3. For the event-aligned comparison in Fig. 3, each bootstrap anomaly series was aligned to the fixed ONI peak month of the corresponding event before the pointwise percentile interval was calculated.

This procedure propagates the estimated random sampling uncertainty of the monthly regional means and the resulting uncertainty in the fitted long-term and seasonal background. It does not include possible common-mode retrieval biases, temporal error covariance among months, or uncertainty arising from incomplete spatial representativeness of the satellite sampling. The resulting intervals should therefore be interpreted as sampling-and-fitting uncertainty rather than total systematic uncertainty in GOSAT XCO_2.

S4.4 Sensitivity to the anomaly-fitting method

As a fitting-method sensitivity test, we additionally calculated anomalies using a calendar-month detrending approach following Chatterjee et al. (6). A separate linear trend was fitted to the observations from each calendar month, and the residuals were treated as anomalies. This alternative method reproduced the principal temporal features obtained with the polynomial–harmonic model, including the early negative anomaly, the subsequent transition to positive values, and the comparatively persistent late response following the 2023/24 event. The interpretation of the event sequence was therefore not dependent on the selected curve-fitting formulation.

S5 Surface-ocean spCO_2 anomalies and comparison with buoy observations

Surface-ocean spCO_2 and air–sea CO_2 flux fields were obtained from the Copernicus Marine Service Surface Ocean Carbon Fields product (product MULTIOBS_GLO_BGC_CARBON_SURFACE_MYNRT_015_008; DOI: 10.48670/moi-00047) (45). This Level-4 product provides monthly reconstructed global fields on a 0.25° × 0.25° grid. We used the multi-year reprocessed dataset (cmems_obs-mob_glo_bgc-car_my_irr-i) and the near-real-time extension (cmems_obs-mob_glo_bgc-car_nrt_irr-i). The Fig. S4 comparison uses the surface seawater partial-pressure field spCO_2 (µatm), not an air–sea flux. Monthly regional means were calculated over Niño 3.4 (5°S–5°N, 170°W–120°W). As an independent consistency check, we compared the Niño 3.4 $spCO_2$ anomaly with atmospheric and seawater pCO_2 observations from the NOAA PMEL TAO mooring at 0°N, 170°W and calculated ΔpCO_2 as seawater pCO_2 minus atmospheric pCO_2 (46, 47). Positive ΔpCO_2 indicates oceanic outgassing, while reduced or near-zero values indicate weakened air–sea CO_2 disequilibrium.

The comparison shows good agreement between the independent buoy observations and the gridded CMEMS product. Both datasets capture the characteristic decline in surface-ocean CO_2 disequilibrium during El Niño development, consistent with suppressed equatorial upwelling and reduced oceanic CO_2 outgassing. The buoy-level validation therefore supports the use of CMEMS Niño 3.4 $spCO_2$ detrended anomalies as a regional diagnostic of the early oceanic component of the ENSO–CO_2 response.

S6 Consistency checks using land-flux, fire-emission and hydroclimate diagnostics

The following diagnostics are provided as supplementary consistency checks for the flux-based interpretation in the main text. They are not used as a formal attribution framework. Instead, they document whether independent fire, ocean-flux and hydroclimate indicators capture the timing and regional structure expected from a delayed post-peak land-carbon response.

We used GFAS v1.2 wildfire overall flux of burnt carbon (cfire) as an independent diagnostic of anomalous fire activity only (29, 30). The native kg m^{-2} s^{-1} field was converted to monthly carbon totals. Monthly anomalies were calculated relative to the 2003–2024 calendar-month climatology. The 2015/16 and 2023/24 El Niño events were aligned to their ONI peaks in December 2015 and December 2023, respectively (lag 0). We evaluated the same six-month windows used in the CAMS v24r1 analysis: pre-peak (lags −6 to −1), early response (0 to +5), and late response (+6 to +11), separately for tropical land (23°S–23°N) and extra-tropical land. CAMS v24r1 covers January 2003–December 2024 in this analysis; the land and ocean variables are flux_apos_bio and flux_apos_ocean, respectively (51).

For tropical land, the late-window GFAS anomaly was -0.108 PgC in 2015/16 and -0.047 PgC in 2023/24; the corresponding late-minus-early changes were -0.249 and +0.015 PgC. For extra-tropical land, late-window anomalies were -0.087 and +0.127 PgC, respectively. Positive anomalies denote increased fire-carbon release. Thus, the late tropical GFAS anomaly was negative in both events, whereas a positive late fire anomaly occurred in the extra-tropics in 2023/24. This pattern does not support increased tropical fire emissions as an explanation for a positive late-phase tropical CAMS NBE anomaly, although extra-tropical fire could contribute to a broader 2023/24 land signal.

GFAS was not added to or subtracted from CAMS net biosphere exchange (NBE), because the CAMS posterior biosphere variable flux_apos_bio already includes fire emissions. GFAS is therefore only a diagnostic fire-emission comparison and not a separate carbon-budget adjustment.

Fig. S6 summarizes the six-month integrated flux anomalies by latitude band and response window. It complements the main-text CAMS analysis by showing how the land, ocean and fire diagnostics vary across the pre-peak, early post-peak and late post-peak periods. This figure is provided in the Supplementary Information because it supports the timing and regional context of the main result without adding a separate attribution claim to the main text.

Fig. S7 shows the corresponding monthly evolution over the tropical band. This time-resolved view helps to identify whether the positive land-flux anomaly is a short pulse or a sustained post-peak feature, and whether it coincides with ocean-flux or fire anomalies. It is included as a supplementary diagnostic because it provides signal detection and a consistency check behind the simplified event-window comparison in the main text.

We further tested whether the delayed post-peak land-flux signal depends on the choice of the early/late window boundary. Within the common observed lag range available for all events, the 2023/24 tropical land-flux anomaly was more concentrated after the first six months than the 2015/16 anomaly. The fraction of positive tropical NBE anomaly occurring during lag +6 to +12 months was 57.3% for 2023/24, compared with 25.1% for 2015/16. This timing contrast was also retained when the early/late boundary was shifted by ±2 months. Using boundaries at lag +4, +6 and +8 months, the corresponding late-phase fractions were 68.7%, 57.3% and 47.6% for 2023/24, compared with 38.4%, 25.1% and 20.7% for 2015/16.

This comparison is used only as a consistency check on the timing of the land-flux signal. The 2023/24 CAMS record currently provides valid event-aligned data only to lag +12 months because the source product ends in December 2024. Therefore, a fully symmetric two-year comparison cannot be made from these products alone. GFAS fire emissions are used as an independent diagnostic and are not added to or subtracted from the CAMS NBE estimates.

Fig. S8 provides hydroclimate context for the land-flux signal using vapor-pressure deficit, precipitation and surface-layer soil moisture anomalies. These variables are not direct carbon-flux constraints and their effects are regionally heterogeneous. The figure is therefore used as supplementary context only, to show whether the environmental background is qualitatively consistent with delayed land-carbon recovery.

Hydroclimate diagnostics were derived from ERA5-Land monthly averaged data on a 0.1° regular grid (53). The source variables were 2-m temperature (t2m), 2-m dewpoint temperature (d2m), total precipitation (tp), and volumetric soil water layer 1 (swvl1). Vapor-pressure deficit was calculated from t2m and d2m; tp was converted from metres to millimetres; and swvl1 represents volumetric soil water ($m^3\ m^{-3}$) in the 0–7 cm surface layer. Monthly anomalies were calculated relative to the corresponding calendar-month climatology.

S7 Data and code availability

All datasets supporting the study are publicly available. ENSO indices and SST were obtained from NOAA CPC ONI and ERSSTv5 (31, 32) and NOAA PSL MEI.v2 (33). Atmospheric CO_2 records were obtained from the NOAA globally averaged marine-surface product, NOAA Mauna Loa, and the Scripps SAM and KUM records (34–36). GOSAT XCO_2 used SWIRL2CO2_GU version 03.05 (37, 38). Palau EM27/SUN data are archived as COCCON PF24 Koror Palau SN032 release R01 (42; https://doi.org/10.48477/coccon.pf24.koror.sn032.r01). IASI/Metop-B total-column CO used ICDR version 6.7.1 (43, 44). Surface-ocean carbon fields came from Copernicus Marine product MULTIOBS_GLO_BGC_CARBON_SURFACE_MYNRT_015_008 (45; https://doi.org/10.48670/moi-00047), with TAO pCO_2 from NOAA PMEL (46, 47). Fire and land-flux diagnostics used GFAS version 1.2 (29, 30), CAMS CO_2 release v24r1 (51), and the GCB2025 gridded 14-inversion ensemble (52; https://doi.org/10.18160/VZ3B-GHYQ). Hydroclimate fields used ERA5-Land monthly averages (53; https://doi.org/10.24381/cds.68d2bb30). Unless otherwise indicated, online products were accessed on 1 July 2026.

Analysis code is archived at Zenodo (https://doi.org/10.5281/zenodo.18676601). No restrictions apply to the data or code beyond the terms specified by the individual providers.

Fig. S1.

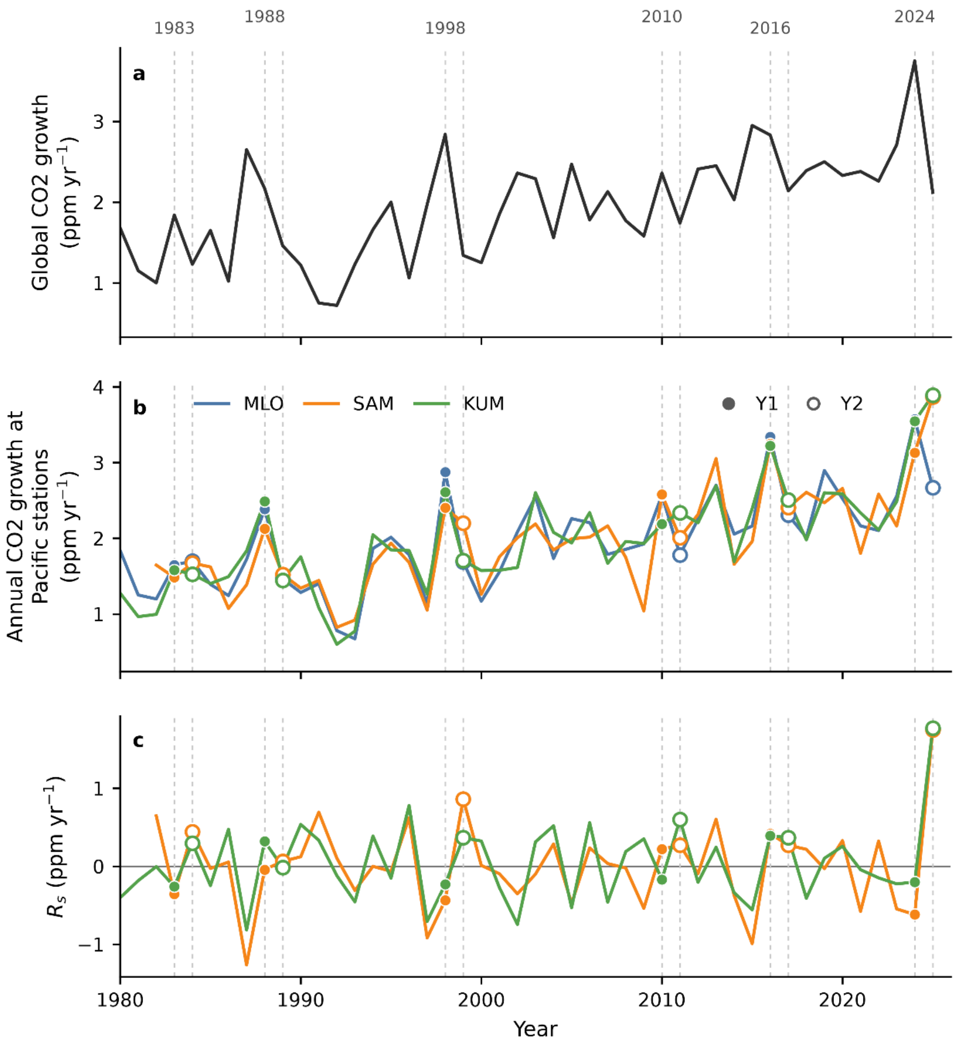

Annual CO2 growth at tropical Pacific background stations.
(a) Annual global CO2 growth rate from the NOAA global mean CO2 record.

(b) Annual CO_2 growth rates at the tropical Pacific background stations American Samoa (SAM) and Cape Kumukahi (KUM), together with Mauna Loa (MLO) as a long-term reference station. Growth rates were calculated as year-to-year differences in full-calendar-year annual mean CO_2 concentrations and assigned to the ending year.

(c) Station-minus-global annual growth anomalies for SAM and KUM, calculated as $R_s(y) = G_{s,y} - G_{\text{global},y}$, where $G_{s,y}$ is the station annual CO_2 growth rate and $G_{\text{global},y}$ is the NOAA global annual CO_2 growth rate for the same ending year. Filled markers denote the ONI peak year (Y1), and hollow markers denote the following post-peak year (Y2) for each selected El Niño event. Vertical dashed lines mark Y1 and Y2; labels above the figure indicate Y1.

Fig. S2.

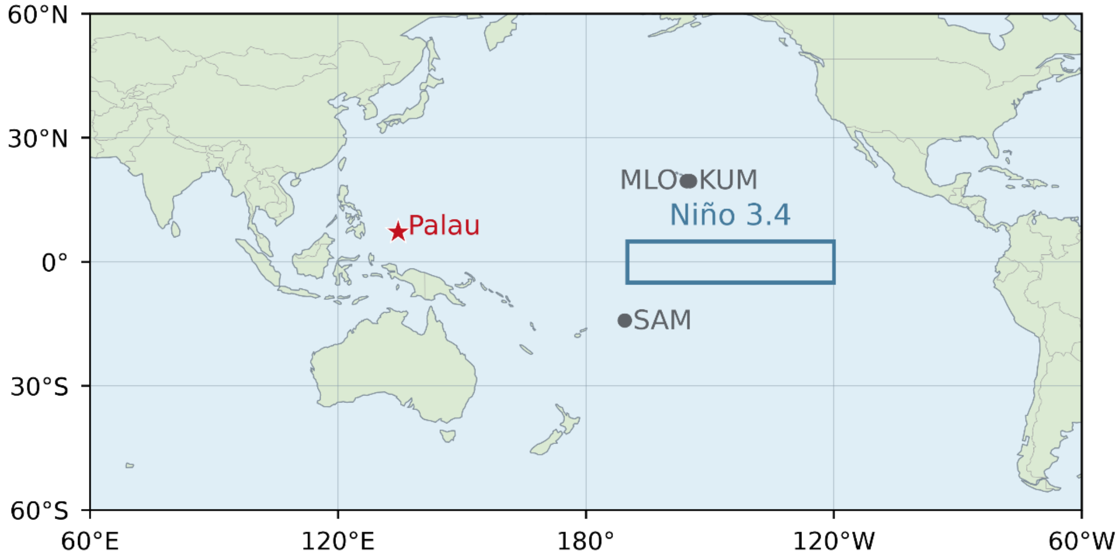

Location of the Palau EM27/SUN site in the tropical western Pacific, the Niño 3.4 region, and reference background CO_2 stations: American Samoa (SAM) and Cape Kumukahi (KUM), together with Mauna Loa (MLO).

Fig. S3

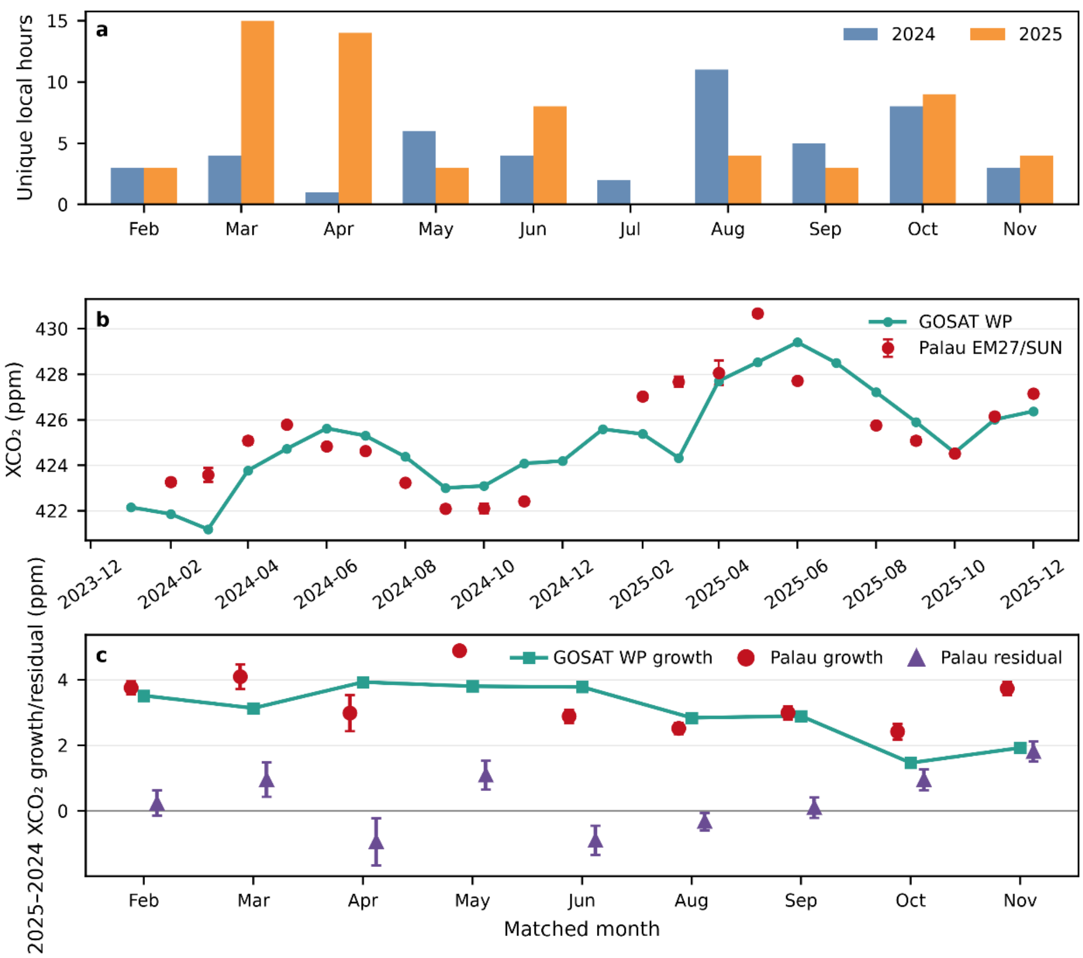

Palau EM27/SUN sampling and residual-growth estimate. (a) Monthly sampling of Palau EM27/SUN observations in 2024 and 2025, expressed as the number of unique local observation hours. (b) GOSAT western Pacific monthly XCO_2 and offset-adjusted Palau EM27/SUN monthly XCO_2. The visual offset does not affect the matched-month growth or residual-growth calculations. (c) Matched-month 2025–2024 growth at Palau, corresponding GOSAT western Pacific background growth, and Palau residual growth after subtracting the GOSAT western Pacific background.

Fig. S4

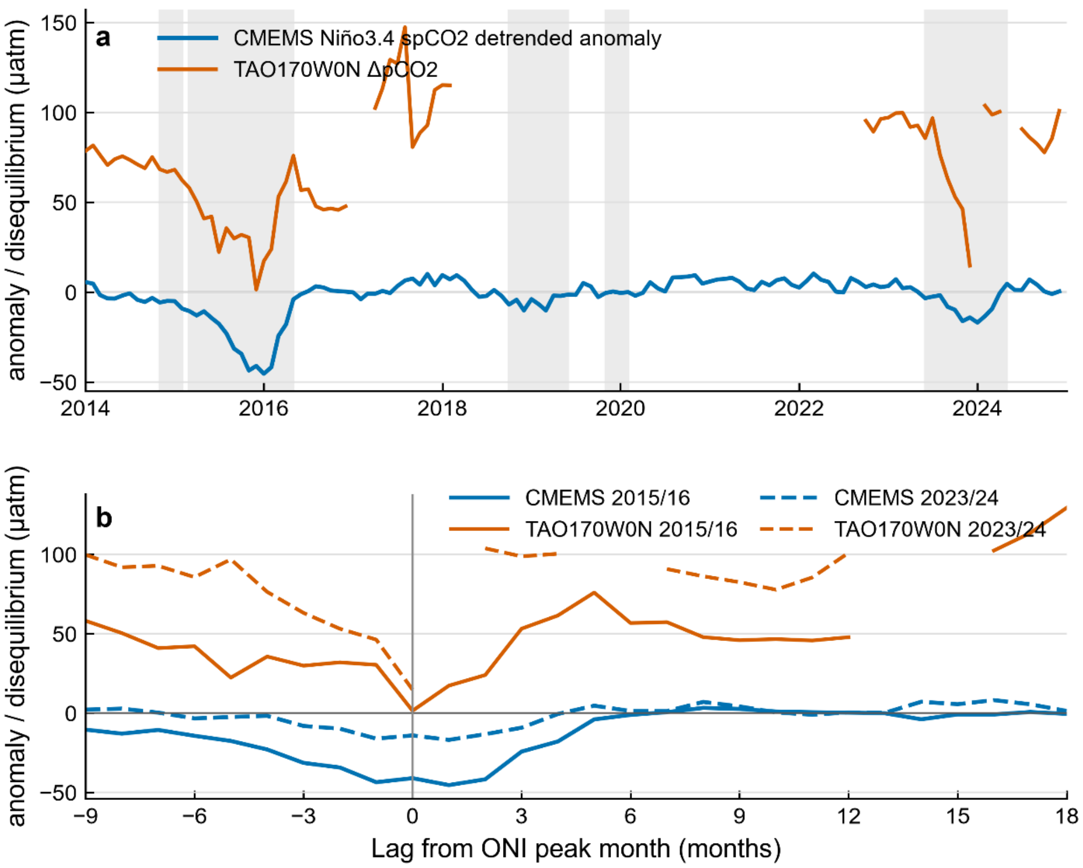

Comparison of Copernicus Marine $spCO_2$ anomalies with TAO buoy ΔpCO_2 in the Niño 3.4 region. (a) Monthly Niño 3.4 regional-mean $spCO_2$ detrended anomalies from the Copernicus Marine Surface Ocean Carbon Fields product compared with in situ ΔpCO_2 observations from the TAO buoy at 0°N, 170°W. The Copernicus Marine anomaly was calculated after removing a fitted linear trend and fixed calendar-month effects from the regional monthly $spCO_2$ time series. TAO ΔpCO_2 is defined as seawater pCO_2 minus atmospheric pCO_2 and is shown as an independent point-based constraint on surface-ocean CO_2 disequilibrium. Grey shading denotes El Niño periods. (b) Event-aligned comparison for the 2015/16 and 2023/24 El Niño events, with lag 0 defined as the ONI peak month. Both datasets show a marked reduction in surface-ocean CO_2 disequilibrium during El Niño development, supporting the Copernicus Marine Niño 3.4 $spCO_2$ anomaly as a regional diagnostic of suppressed equatorial upwelling and reduced oceanic CO_2 outgassing.

Fig. S5

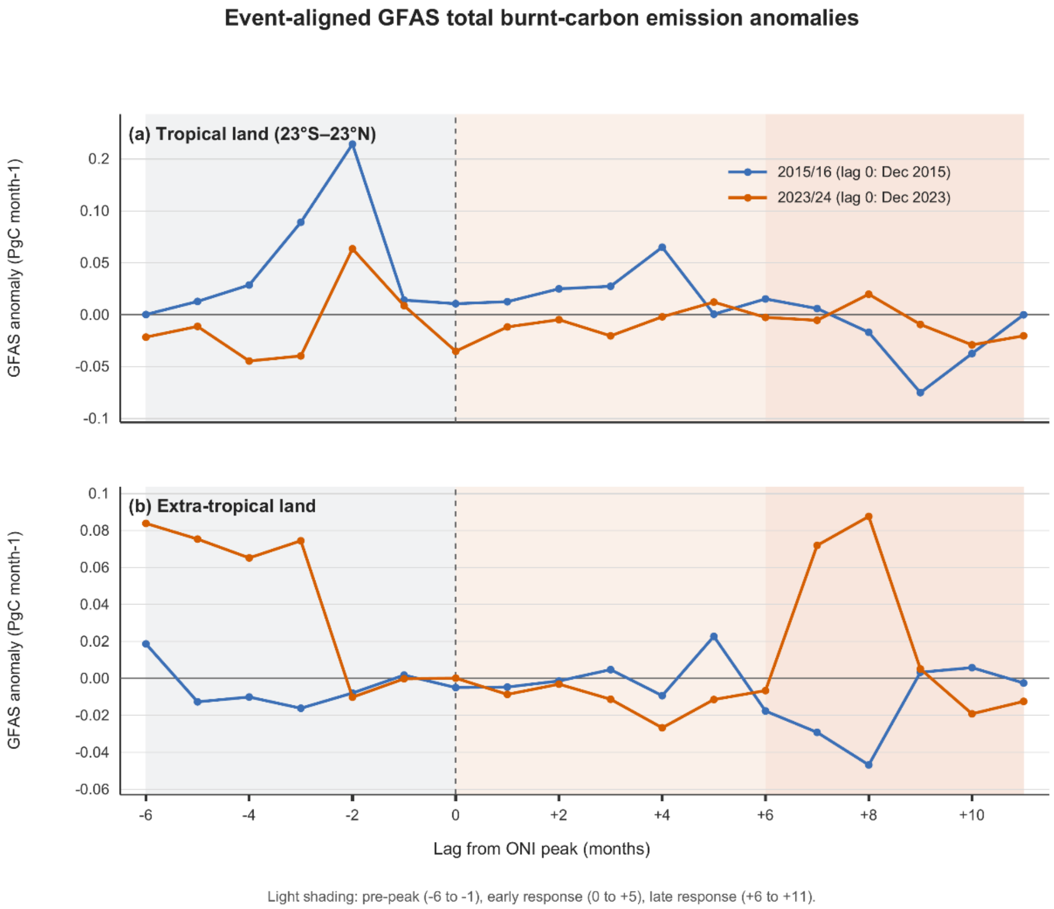

Event-aligned GFAS total burnt-carbon emission anomalies. Monthly total burnt-carbon emission anomalies from the Global Fire Assimilation System (GFAS) are shown for tropical land (23°S–23°N) and extra-tropical land during the 2015/16 and 2023/24 El Niño events. Each event is aligned to the month of maximum ONI, defined as lag 0, corresponding to December 2015 and December 2023, respectively. Blue, orange and green shading mark the pre-peak period (lags −6 to −1), early post-peak response (lags 0 to +5), and late post-peak response (lags +6 to +11). Positive values indicate enhanced fire carbon emissions relative to the monthly climatology, whereas negative values indicate reduced emissions. GFAS is used here as an independent fire diagnostic and is not added to the CAMS net biosphere exchange because fire emissions are already included in the posterior biosphere flux.

Fig. S6

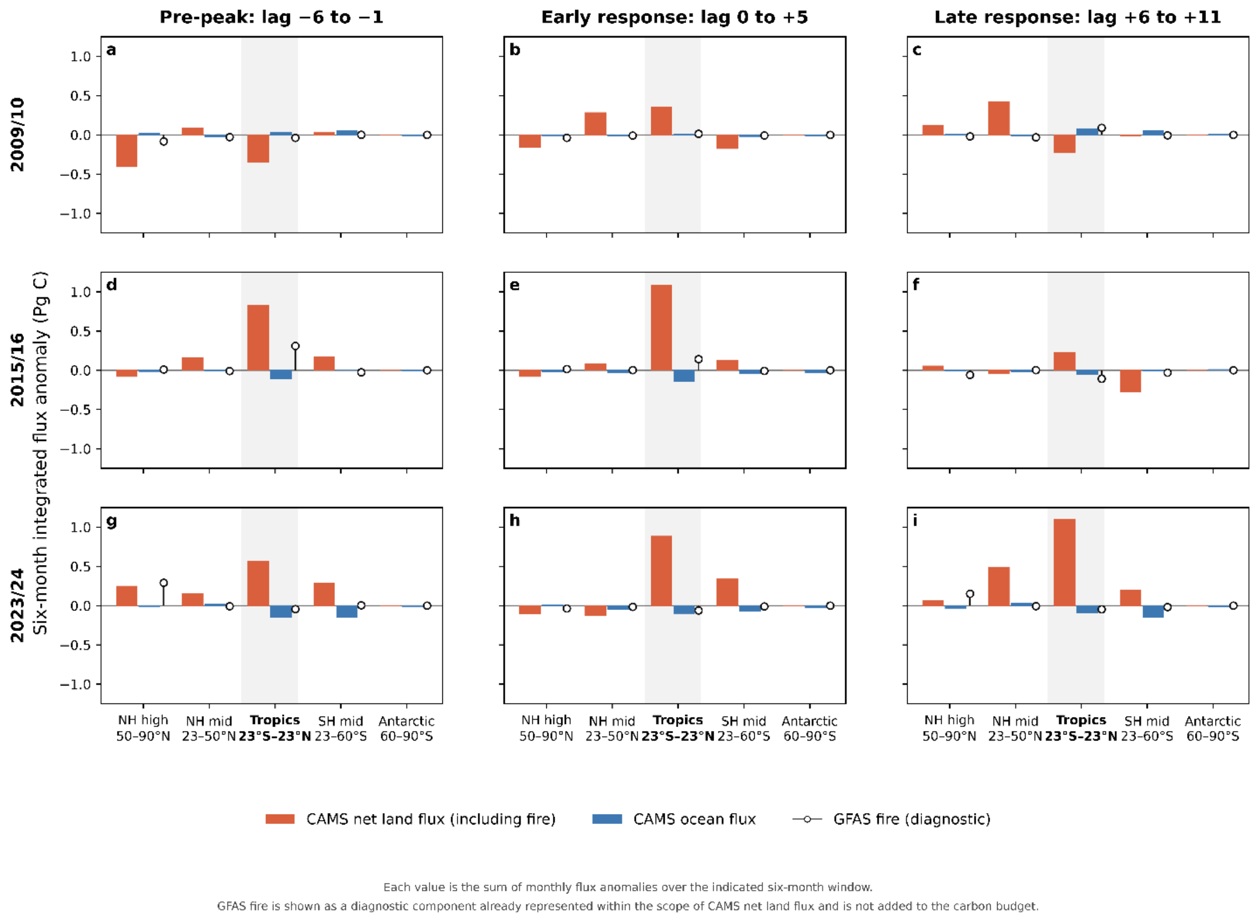

Six-month integrated CAMS land and ocean flux anomalies and GFAS fire-emission anomalies by latitude band. Rows show the 2009/10, 2015/16 and 2023/24 El Niño events, and columns show the pre-peak period (lags −6 to −1), early post-peak response (lags 0 to +5) and late post-peak response (lags +6 to +11), with lag 0 defined as the ONI peak month. Bars show CAMS net land flux, including fire, and CAMS ocean flux integrated over each six-month window. Black markers show GFAS total burnt-carbon emissions as an independent diagnostic of fire activity. The grey band highlights the tropical latitude band (23°S–23°N). Positive land-flux anomalies indicate enhanced net CO_2 release to the atmosphere or reduced land uptake, whereas positive GFAS anomalies indicate enhanced fire-carbon emissions. GFAS is shown only as a diagnostic and is not added to the CAMS net land flux, because fire emissions are already included in the CAMS posterior biosphere flux.

Fig. S7

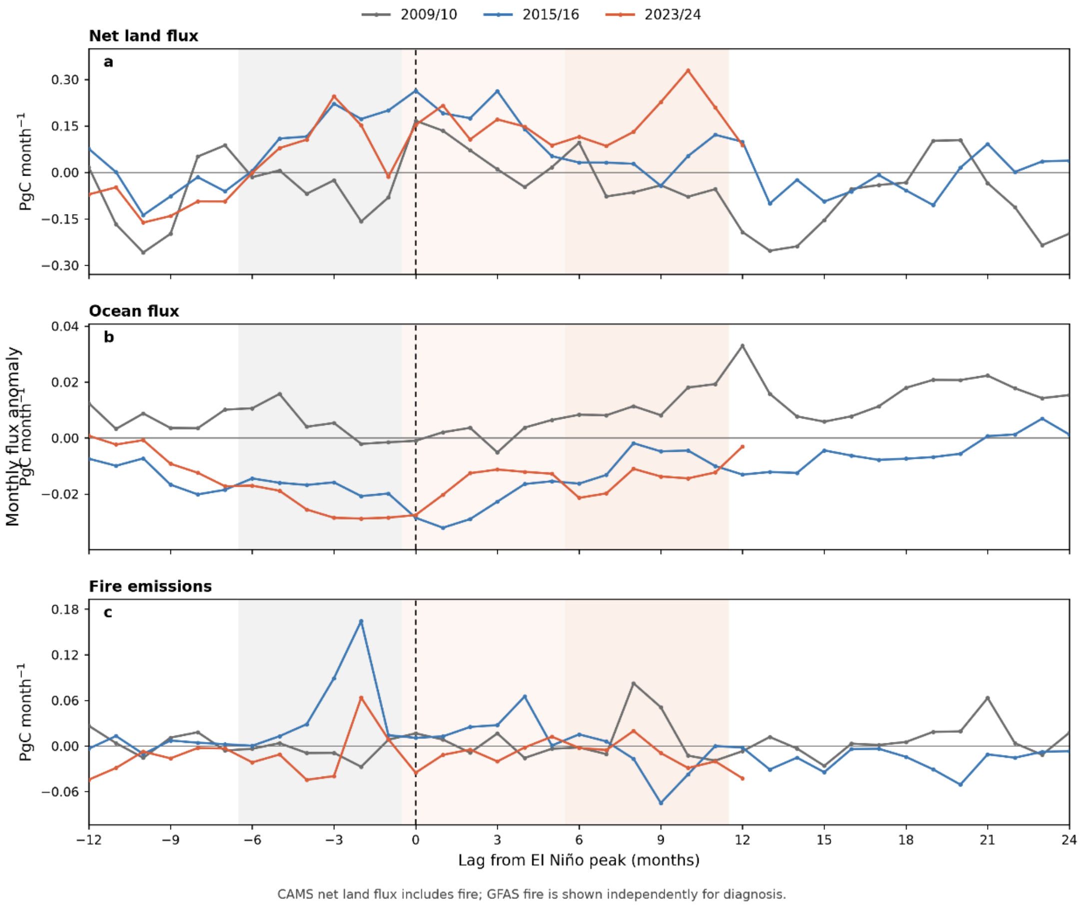

Event-aligned monthly CAMS flux and GFAS fire diagnostics over the tropical band. Monthly anomalies are shown for the 2009/10, 2015/16 and 2023/24 El Niño events, aligned to the ONI peak month at lag 0. (a) CAMS net land flux, including fire, over tropical land, (b) CAMS ocean flux over the tropical ocean, and (c) GFAS total burnt-carbon emissions over tropical land. Grey shading denotes the pre-peak window (lags −6 to −1), and light orange shading denotes the post-peak window emphasized in the CAMS analysis (lags 0 to +11). The figure provides a time-resolved consistency check showing that the 2023/24 positive tropical land-flux anomaly persists after the ENSO peak, while the ocean-flux anomaly remains comparatively small and GFAS fire emissions do not show a matching sustained tropical increase.

Fig. S8.

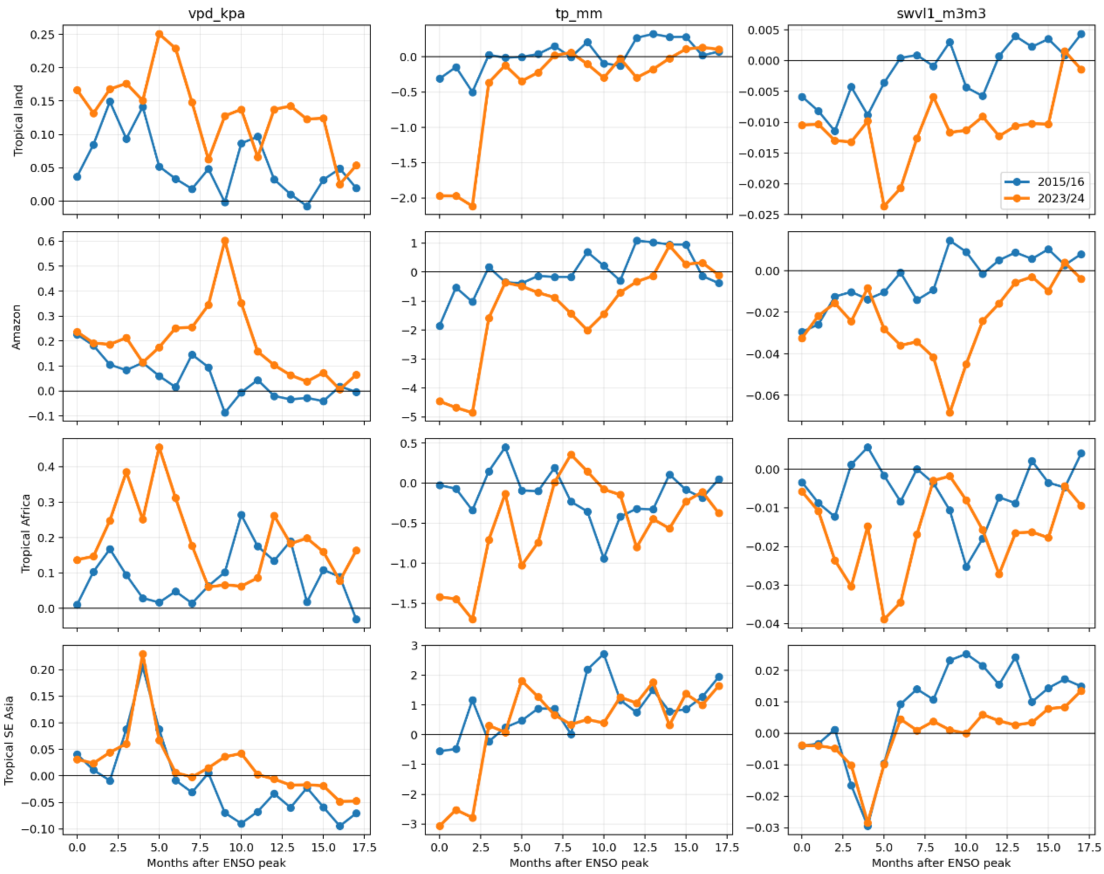

Event-aligned hydroclimate anomalies over tropical land and selected tropical regions. Rows show tropical land, the Amazon, tropical Africa and tropical Southeast Asia. Columns show vapor-pressure deficit (VPD; kPa), total precipitation (tp; mm) and surface-layer volumetric soil water (swvl1; m^3 m^{-3}). Blue and orange lines show the 2015/16 and 2023/24 El Niño events, respectively, with month 0 defined as the ONI peak month. Anomalies are calculated relative to the corresponding calendar-month climatology. The diagnostics indicate that the 2023/24 event was accompanied by higher atmospheric dryness and reduced near-surface soil moisture in several tropical regions after the ENSO peak. These hydroclimate anomalies provide environmental context for the delayed land-carbon signal, but are used here only as qualitative supporting evidence rather than as a quantitative attribution analysis.

Fig. S9

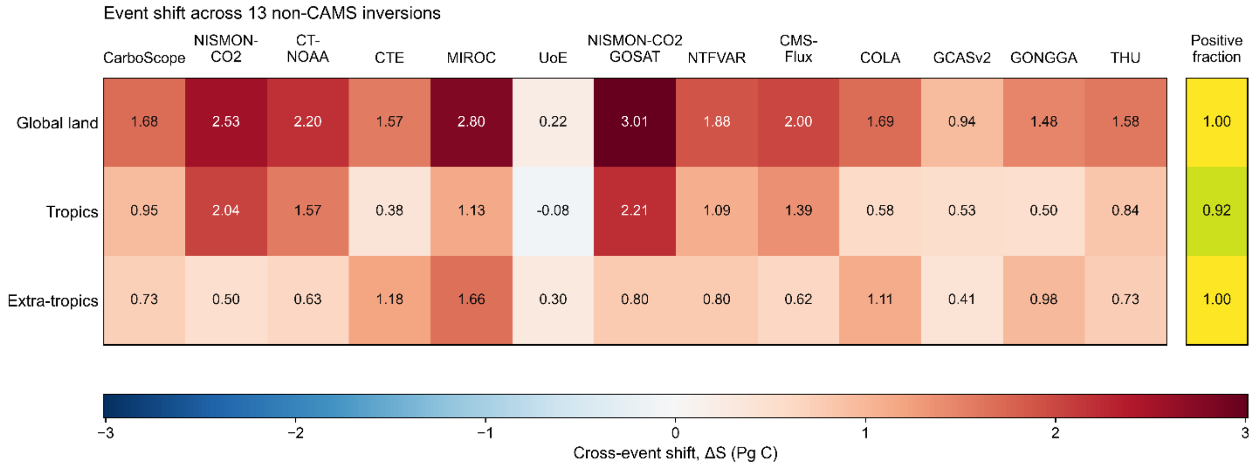

Cross-inversion consistency of the event shift in land net biosphere exchange. For each of 13 non-CAMS atmospheric CO_2 inversions, the event shift was calculated as

$$\Delta S = [\text{late} - \text{early}]_{2023/24} - [\text{late} - \text{early}]_{2015/16},$$

where the early and late periods correspond to lags 0 to +5 and +6 to +11 months relative to the El Niño peak, respectively. Values are spatially integrated over global land, the tropics (23°S–23°N), and the extratropics and are reported in Pg C. Positive values indicate a stronger shift toward late land-to-atmosphere carbon release during 2023/24 than during 2015/16. The right column shows the fraction of inversion products with $\Delta S > 0$.

Table S1. El Niño peak months used for event alignment.

Event	Peak month
1982/83	1982-12
1987/88	1987-08
1991/92	1992-01
1994/95	1994-12
1997/98	1997-11
2002/03	2002-11
2004/05	2004-09
2006/07	2006-11
2009/10	2009-12
2015/16	2015-12
2018/19	2018-11
2023/24	2023-12

Table S2. Event-masked LOWESS threshold sensitivity.

Event	D0.25 (months)	D0.33 (months)	D0.50 (months)
1982/83	10	6	5
1987/88	15	12	7
1991/92	0	0	0
1994/95	5	4	3
1997/98	13	13	11
2002/03	11	11	7
2004/05	12	9	8
2006/07	5	5	4
2009/10	6	5	5
2015/16	7	7	6
2018/19	5	3	3
2023/24	**12**	**11**	**10**

Table S3. Full event-masked LOWESS results for the 12 events.

Event	Peak anomaly (ppm yr−1)	Peak lag (months)	D0.50 (months)	I18 (ppm)
1982/83	1.038	2	5	0.506
1987/88	1.371	0	7	0.993
1991/92	-0.146	19	0	-1.261
1994/95	0.986	13	3	0.338
1997/98	1.938	4	11	1.361
2002/03	1.042	1	7	0.532
2004/05	0.780	11	8	0.424
2006/07	0.539	14	4	-0.007
2009/10	0.591	4	5	-0.075
2015/16	1.323	2	6	0.431
2018/19	0.306	5	3	0.001
2023/24	**1.193**	**7**	**10**	**0.885**

Table S4. Event-masked LOWESS cumulative-window sensitivity (ppm).

Event	I12	I15	I18	I21
1987/88	0.872	1.004	0.993	0.929
1997/98	1.311	1.422	1.361	1.281
2009/10	0.154	0.071	-0.075	-0.173
2015/16	0.678	0.589	0.431	0.383
2023/24	**0.897**	**0.923**	**0.885**	**0.762**

Table S5. Residual fitting diagnostics.

Method	Residual variance	Lag-1 autocorrelation
Current	0.478248	0.960298
Linear	0.293828	0.935244
Quadratic	0.291141	0.934620
Cubic	0.291114	0.934623
Quartic	0.290996	0.934608
10-year LOWESS	0.256199	0.925565
Event-masked LOWESS	0.294286	0.935415
GCV cubic spline	**0.057282**	**0.710523**

Table S6. Annual CO_2 growth rates and station-minus-global anomalies during post-peak years of selected El Niño events since 1980.

Event	1982/83	1987/88	1997/98	2009/10	2015/16	2023/24
Post-peak year	1984	1989	1999	2011	2017	2025
Global growth (ppm yr^{-1})	1.23	1.46	1.34	1.74	2.14	2.12
MLO growth (ppm yr^{-1})	1.70	1.46	1.69	1.78	2.30	2.67
SAM growth (ppm yr^{-1})	1.67	1.523	2.20	2.01	2.40	3.87
KUM growth (ppm yr^{-1})	1.52	1.44	1.70	2.33	2.50	3.89
SAM R_s (ppm yr^{-1})	0.44	0.06	0.86	0.27	0.26	1.75
KUM R_s (ppm yr^{-1})	0.29	-0.02	0.36	0.59	0.36	1.77

Table S7. Summary of the sensitivity of the Palau matched-month annual growth estimate.

Test	Months used	N	Growth estimate	Difference from the default
Default: equal-day weighting, all matched months	Feb, Mar, Apr, May, Jun, Aug, Sep, Oct, Nov	9	3.36 ± 0.09	0.00
Retrieval-weighted means	Same as default	9	3.29 ± 0.01	−0.07
≥2 independent days in both years	Mar, Oct	2	3.25 ± 0.23	−0.11
Months through Aug 2025 only	Feb, Mar, Apr, May, Jun, Aug	6	3.52 ± 0.13	+0.16
Leave-one-month-out range	8 months each	8	3.17–3.48	−0.19 to +0.12

Table S8. GOSAT spatial domains used in the analysis.

Region	Latitude	Longitude	Application
Niño3.4	5°S–5°N	170°W–120°W	Fig. 2C
Western Pacific	5°S–5°N	120°E–180°E	Palau background
Tropical Pacific	10°S–10°N	110°E–90°W	Fig. 3A
Global	90°S–90°N	All longitudes	Fig. 3B

Table S9 Atmospheric CO_2 inversion products used for the primary land-flux analysis and cross-inversion consistency assessment.

Product and version	Assimilated CO_2 observations	Atmospheric transport model	Meteorological forcing	Land-biosphere prior and prescribed fire flux	Native transport resolution	Use in this study	Primary reference
CAMS global CO_2 inversion, surface-air-sample release v24r1	Surface and aircraft air-sample measurements	LMDz/PYVAR	ERA5 horizontal winds	ORCHIDEE climatological biosphere prior with prescribed fire fluxes	Hexagonal grid, approximately 90 km	Primary temporal and spatial land-flux analysis	CAMS global inversion-optimized greenhouse-gas fluxes, doi:10.24381/ed2851d2
Jena CarboScope r76nbetEXToc_v2025	Surface in situ observations	TM3	ERA5	Zero biospheric prior	4° × 6°	Cross-inversion consistency assessment	Friedlingstein et al. (2026); Luijkx et al., doi:10.18160/VZ3B-GHYQ
NISMON-CO_2 v2025.1	Surface in situ observations	NICAM-TM	JRA-3Q	VISIT with GBEI fire emissions	glevel-5, approximately 223 km	Cross-inversion consistency assessment	Friedlingstein et al. (2026); Luijkx et al., doi:10.18160/VZ3B-GHYQ
CarbonTracker NOAA CT2025	Surface in situ observations	TM5	ERA5	MiCASA v1 with GFEDv3 fire emissions	Global 3° × 2°, with a 1° × 1° North American nest	Cross-inversion consistency assessment	Friedlingstein et al. (2026); Luijkx et al., doi:10.18160/VZ3B-GHYQ

Product and version	**Assimilated CO_2 observations**	**Atmospheric transport model**	**Meteorological forcing**	**Land-biosphere prior and prescribed fire flux**	**Native transport resolution**	**Use in this study**	**Primary reference**
CarbonTracker Europe CTE2025	Surface in situ observations	TM5	ECMWF meteorological fields	SiB4-MERRA with GFAS fire emissions	Global 3° × 2°, with 1° × 1° European and North American nests	Cross-inversion consistency assessment	Friedlingstein et al. (2026); Luijkx et al., doi:10.18160/VZ3B-GHYQ
MIROC-ACTM v2025	Surface in situ observations	MIROC-ACTM	JRA-3Q	MiCASA with GFED4s fire emissions	2.8° × 2.8°	Cross-inversion consistency assessment	Friedlingstein et al. (2026); Luijkx et al., doi:10.18160/VZ3B-GHYQ
University of Edinburgh inversion v2025	OCO-2 XCO_2 retrievals	GEOS-Chem	MERRA meteorological fields	CASA v1.0, climatological after 2016, with GFED4.0 fire emissions	2° × 2.5°	Cross-inversion consistency assessment	Friedlingstein et al. (2026); Luijkx et al., doi:10.18160/VZ3B-GHYQ
NISMON-CO_2 GOSAT v2025.1	GOSAT XCO_2 retrievals	NICAM-TM	JRA-3Q	VISIT with GBEI fire emissions	glevel-5, approximately 223 km	Cross-inversion consistency assessment	Friedlingstein et al. (2026); Luijkx et al., doi:10.18160/VZ3B-GHYQ

Product and version	**Assimilated CO_2 observations**	**Atmospheric transport model**	**Meteorological forcing**	**Land-biosphere prior and prescribed fire flux**	**Native transport resolution**	**Use in this study**	**Primary reference**
NTFVAR v2025	Surface in situ observations and GOSAT XCO_2 retrievals	NIES-TM–FLEXPART	ERA5 for NIES-TM and JRA-55 for FLEXPART	Zeng et al. biosphere prior with GFAS fire emissions	NIES-TM: 3.75° × 3.75°; FLEXPART: 0.1° × 0.1°	Cross-inversion consistency assessment	Friedlingstein et al. (2026); Luijkx et al., doi:10.18160/VZ3B-GHYQ
CMS-Flux member submitted to GCB2025	Surface in situ observations and OCO-2 XCO_2 retrievals	GEOS-Chem	MERRA2	CARDAMOM; fire emissions based on GFED4.1 before 2024 and GFAS in 2024	4° × 5°	Cross-inversion consistency assessment	Friedlingstein et al. (2026); Luijkx et al., doi:10.18160/VZ3B-GHYQ
COLA v2025	Surface in situ observations and OCO-2 XCO_2 retrievals	GEOS-Chem v13.0.2	MERRA-2	VEGAS with GFAS fire emissions	2° × 2.5°	Cross-inversion consistency assessment	Friedlingstein et al. (2026); Luijkx et al., doi:10.18160/VZ3B-GHYQ
GCASv2 v2025	OCO-2 XCO_2 retrievals	MOZART-4	GEOS-5	BEPS with GFED4.1s fire emissions	2.5° × 1.875°	Cross-inversion consistency	Friedlingstein et al. (2026); Luijkx et al., doi:10.18160/VZ3B-

Product and version	Assimilated CO_2 observations	Atmospheric transport model	Meteorological forcing	Land-biosphere prior and prescribed fire flux	Native transport resolution	Use in this study	Primary reference
						assessment	GHYQ
GONGGA v2025	OCO-2 XCO_2 retrievals	GEOS-Chem v12.9.3	MERRA2	ORCHIDEE-MICT with GFED4.1s fire emissions	2° × 2.5°	Cross-inversion consistency assessment	Friedlingstein et al. (2026); Luijkx et al., doi:10.18160/VZ3B-GHYQ
Tsinghua University inversion v2025	OCO-2 XCO_2 retrievals	GEOS-Chem v12.2	GEOS-FP	SiB4.2 with GFED4.1s fire emissions	4° × 5°	Cross-inversion consistency assessment	Friedlingstein et al. (2026); Luijkx et al., doi:10.18160/VZ3B-GHYQ

Note. CAMS v24r1 was used for the primary temporal and spatial land-flux analyses and covered January 2003 to December 2024. The remaining 13 products were ensemble members of the harmonized GCB2025 gridded atmospheric-inversion product and covered January 2003 to November 2024. The CAMS-Satellite member of the GCB2025 product was excluded because the separate CAMS v24r1 surface-observation inversion was analyzed independently. Within GCB2025, differences in fossil-fuel and cement fluxes were adjusted to GridFED v2025.1, including the cement-carbonation sink. The separate CAMS v24r1 product was not subjected to this additional adjustment. All products were analyzed as monthly fields on a common 1° × 1° grid. CAMS required longitude reordering but no spatial interpolation. The inversion products are not fully independent because some share atmospheric observations, transport frameworks, meteorological forcing, prior flux information, or GCB2025 harmonization choices. Positive posterior land flux denotes net carbon transfer from land to the atmosphere.